Materials Characterization 229 (2025) 115529

Contents lists available at ScienceDirect

Materials Characterization

journal homepage: www.elsevier.com/locate/matchar

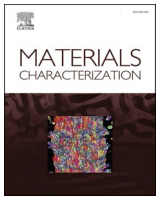

Characterisation by phase mappings of microstructural-thermal-mechanical properties in equimolar refractory high-entropy alloys with reduced neutron cross-section

P.A. Ferreirós [a,b,*], K. Ma [a,c,**], C. Bearcroft [d,e], A.J. Cackett [f], K. Aryana [g], M.S.B. Hoque [g], P.E. Hopkins [g,h,i], A.J. London [d], A.J. Knowles [a,d,***]

[a] School of Metallurgy and Materials, University of Birmingham, Birmingham B15 2TT, UK
[b] Advanced materials for nuclear energy, VTT Technical Research Centre of Finland Ltd, Espoo 02150, Finland
[c] Department of Mechanical Engineering, City University of Hong Kong, Hong Kong, China
[d] Materials Research Facility, UK Atomic Energy Authority, Culham Campus, Oxfordshire OX14 3DB, UK
[e] Idaho National Laboratory, Idaho Falls, ID, USA
[f] National Nuclear Laboratory, Culham Campus, Abingdon, Oxfordshire OX14 3DB, UK
[g] Department of Mechanical and Aerospace Engineering, University of Virginia, Charlottesville, VA, USA
[h] Department of Materials Science and Engineering, University of Virginia, Charlottesville, VA, USA
[i] Department of Physics, University of Virginia, Charlottesville, VA, USA

ARTICLE INFO

Keywords:
HEA
Nuclear application
Mapping techniques
Scanning electron microscopy
Thermal conductivity
Nanoindentation

ABSTRACT

High-entropy alloys (HEA) hold promising potential as advanced technology fuel cladding materials for nuclear fission reactors. The HEAs typically exhibit low thermal conductivity, influencing substantially thermal spikes caused by nuclear collisions. In this framework, we screened over fifteen million combinations of quaternary and quinary equimolar HEAs to select the best alloy candidates for lower thermal neutron absorption cross-section combined with propensity to form a single-phase solid solution at high temperatures. Three of these HEAs NbZrTiMo, NbZrTiVMo, and NbZrTiV were arc-melted and characterised after thermal annealing at 1200 °C for 100 h. While a single-phase field was not achieved, each alloy exhibited a predominant bcc phase. We employed a unique combination of co-located advanced mapping techniques, including scanning electron microscopy, time-domain thermoreflectance (TDTR), and nanoindentation. High-resolution TDTR mapping was integrated with conventional mapping techniques (SEM, EDS, EBSD, and nanoindentation) to produce a micrometre-scale profile of the material properties. This multi-technique approach enabled a detailed characterisation of each phase, covering aspects such as phase size, morphology, distribution, crystalline orientation, chemical composition, thermal conductivity, nanohardness, and elastic modulus. The insights gained from this comprehensive characterisation provide a strong foundation for further HEAs optimisation, including efforts to enhance beneficial phases and suppress undesired ones.

1. Introduction

A new alloy design paradigm emerged in 2004 with the introduction of the high-entropy alloy (HEA) concept [1,2]. The creation of a multi-principal element alloy design removed the limitation of a traditional design strategy based on a single principal element. Consequently, an immense new range of alloy design possibilities were opened up. The vast compositional search space offers significant potential for diverse fields, and some are already showing outstanding properties compared to conventional alloys [3–6]. The development of structural materials for extreme environments, such as nuclear fusion and fission applications, demands alloys with exceptional properties, which HEAs are well-positioned to provide [7–10]. Fig. 1 illustrates the rapid growth of HEAs in focused scientific publications over their two decades since their

* Correspondence to: P.A. Ferreirós, VTT Technical Research Center Ltd, Kivimiehentie 3, 02150 Espoo, Finland.
** Correspondence to: K. Ma, Department of Mechanical Engineering, City University of Hong Kong, Hong Kong, China.
*** Correspondence to: A.J. Knowles, Metallurgy & Materials, University of Birmingham, Elms Road, Edgbaston, Birmingham B15 2SE, UK.
E-mail addresses: Pedro.Ferreiros@vtt.fi (P.A. Ferreirós), kan.ma@cityu.edu.hk (K. Ma), a.j.knowles@bham.ac.uk (A.J. Knowles).

https://doi.org/10.1016/j.matchar.2025.115529
Received 15 May 2025; Received in revised form 31 August 2025; Accepted 2 September 2025
Available online 10 September 2025

conception. It can be observed that both "refractory HEAs" and "nuclear application HEAs" have also experienced tremendous growth in scientific publications. In fission reactors, zirconium-based alloys have historically been the leading fuel cladding material [11]. Their two outstanding properties are low thermal neutron absorption cross-section and high corrosion resistance. On the other hand, the disadvantage of these alloys is the potential for catastrophic failure at elevated temperatures in the event of a loss-of-coolant accident. To mitigate this potential failure, new alloys are being sought under the concept of advanced technology fuels (ATF) [12], and this is where HEAs could offer a superior solution. To this end, one of the HEA design targets selected in this work is a reduced macroscopic thermal neutron absorption cross-section (Σ). The Σ could be calculated as follows;

$$\Sigma = \frac{\rho N_a}{M}\sum_i (C_i\sigma_i) \quad (1)$$

where ρ is the density of the compound, N_a is Avogadro's number, M is the molecular weight of the compound and σ_i is the neutron absorption cross-section of ith element which in this case was evaluated for thermal neutrons (25.3 meV).

While the concept of HEAs was initially developed with the objective of creating single-phase alloys, the focus has since shifted toward introducing secondary reinforcing phases to enhance their properties [13]. Nevertheless, for the production and processing of HEAs, maintaining a single-phase structure at elevated temperatures offers distinct advantages. It enables the implementation of thermal treatments, such as homogenization, and facilitates the application of thermomechanical forming techniques. Therefore, a second alloy design target in the present work is to obtain a single-phase field at high temperatures. The two selected targets limit the results to the alloys that fall within the intersection of both sets. Even though second phases are likely to form at lower application temperatures, allowing precipitation hardening., King et al. [14] developed an empirical criterion for HEAs which predicts a stable single-phase solid solution below the melting temperature. The criterion used 2 parameters, the Φ parameter and the atomic radius mismatch (δ) between elements. The condition for the formation of a single-phase solid solution below melting temperature is: $\Phi \geq 1$ and $\delta < 6.6$ %. While similar to the widespread empirical criterion of Yang et al. [15], this is improved because it considers the change in Gibbs free energy of formation of the disordered solid solution, ΔG_{ss}, and the intermetallic or segregated binary constituents, ΔG_{max}. The parameters are calculated as follows:

$$\Phi = \frac{\Delta G_{ss}}{-|\Delta G_{max}|} \& \delta[\%] = \sqrt{\sum_{i=1}^{n} C_i\left(1-\frac{r_i}{\bar{r}}\right)^2}\, x100 \quad (2)$$

where C_i and r_i are the atomics percentage and radius of element i respectively, and $\bar{r}$ is the atomic radius average of the system.

Due to the vast combinatorial space of HEAs, their design requires computational techniques to minimize the number of possibilities and find a narrowed set that satisfies the target properties [16–18]. In this work, the Alloy Search and Predict (ASAP) code [19] is used as a screening tool to assess quaternary and quinary equimolar element combinations (≈15 million combinations). The two parameters (δ and Φ) required to predict the single-phase stability at high temperatures were obtained for each combination using the ASAP code. Building on the work of King et al. who used similar screening methods to obtain HEAs with reduced microscopic neutron cross-sections (σ_{alloy}) [20], this work advances the approach by targeting a reduced macroscopic cross-section (Σ) instead. This shift in focus considers the alloy density, making Σ a more relevant metric for the application.

To verify the structural and property predictions for the selected HEAs, it is crucial to assess their phase composition directly—particularly to determine if they achieve the targeted single-phase structure, as phase diagram calculations often show discrepancies in HEAs. Additionally, understanding the presence and role of any thermodynamically stable secondary phases after thermal annealing is essential to evaluate their influence on overall material performance. To achieve this, we employed a unique combination of advanced mapping techniques, including scanning electron microscopy, time-domain thermoreflectance (TDTR), and nanoindentation, applied to the same sample regions. Given that HEAs typically exhibit low thermal conductivity—strongly impacting the thermal spikes caused by nuclear collisions [21] —this aspect was a particular focus. For the first time, we

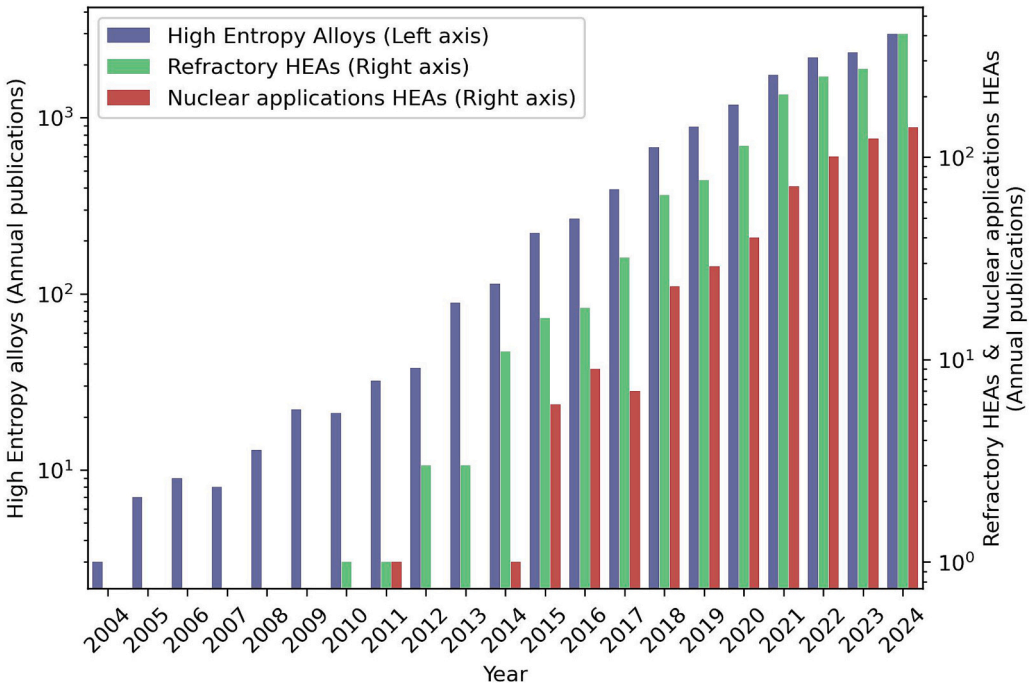

Fig. 1. Growth of publications on HEAs, by year, spanning the two decades since their discovery, as well as the growth in those for nuclear applications and refractory HEAs (RHEAs). Source search engine method in Supplementary material.

integrated high-resolution TDTR mapping with conventional mapping techniques (SEM, EDS, EBSD, and nanoindentation) to produce a detailed profile of the material properties at the micrometre scale. This multi-technique approach enabled a detailed characterisation of each phase, covering aspects such as phase size, morphology, distribution, crystalline orientation, chemical composition, thermal conductivity, hardness, and elastic modulus. The insights gained from this comprehensive characterisation provide a strong foundation for further optimisation, including efforts to enhance beneficial phases and suppress undesired ones in future work.

2. Material and methods

The ASAP code [19] was used as a screening tool to assess equimolar quaternary and quinary combinations of 72 elements of the periodic table (see Supplementary material Fig. S1).

Phase equilibrium calculation between 730 K and 2550 K was performed by the Calculations of PHAse Diagram (CALPHAD) method in Thermocalc™ with the TCHEA6 database.

Three equimolar alloys, with compositions given in Table 1, were prepared by arc melting of elemental metals with purity ≥99.9 wt%. The ingots were performed with a careful strategy of successive melting steps. Final ingots of about 8 g were obtained with sequences of between 3 and 15 steps and up to a maximum of 3 chamber openings. The chamber was evacuated, Ar-backfilled and a Ti lump melted as a remaining gas getter. The melting strategy consists of using the higher melting point elements in the first steps and gradually adding the other elements to progressively lower the melting point of the intermediate alloy, reaching the target composition in the final steps when the lowest melting point element is added. In addition, the ingot was inverted and remelted 3 to 5 times in each step to homogenise the melt. The quinary alloy required the largest number of steps, with over 50 remeltings. For heat treatments, samples were wrapped in Mo foil and encapsulated in a silica glass evacuated and backfilled with Ar gas. As-cast alloys were homogenized at 1200 °C for 100 h and water quenched. The densities were measured in half ingots by the Archimedes method.

The X-ray diffraction (XRD) patterns were taken on a Proto AXRD benchtop diffractometer (Cu K_α radiation) using 0.015° step size and spinning sample holder. The background subtracted spectra are presented in the XRD results. Hardness was measured by Vickers testing using a 1000 g load in a Mitutoyo HM-124. Scanning Electron Microscopy (SEM) was performed in a Jeol 7000F with Oxford Inca energy-dispersive X-ray spectroscopy (EDS) and electron backscatter diffraction (EBSD) detectors, operated at 20 kV accelerating voltage. Surfaces for SEM were prepared by grinding and polishing with SiC papers & colloidal silica. Alloy compositions were calculated as an average of six EDS area scans (about 2×10^{-2} mm^2) widely spaced over a central slice of the homogenized ingot. Phase compositions were calculated as an average of six to ten point EDS measurements. Standard deviations are reported together with the results. EBSD maps were made with a step size of 0.2 μm. Phase fractions were obtained from EBSD measurements using Aztec 6.1. The EBSD technique did not distinguish between the two bcc phases, but by analysing the grain sizes it was possible to split the bcc area into two, where bcc1 covers large areas with large grain size (only a few grains), and the remainder area for small grains of bcc2. In addition, backscattered electrons (BSE), as opposed to secondary electrons (SE), allows the bcc2 phase to be distinguished from the bcc1 phase by their dark colour. The EBSD areas analysed were 8×10^4 μm^2, 6×10^4 μm^2, and 1×10^5 μm^2, for NbZrTiMo, NbZrTiVMo, and NbZrTiV alloys respectively.

Table 1
Alloy designations, target compositions, and compositions measured by EDS area scans.

Alloy	Target composition	Measured composition (at. %)				
		Nb	Zr	Ti	V	Mo
1	NbZrTiMo	24.4 ± 0.3	25.6 ± 0.3	25.3 ± 0.2	–	24.7 ± 0.2
2	NbZrTiVMo	20.0 ± 0.0	20.1 ± 0.1	20.1 ± 0.1	19.7 ± 0.1	19.7 ± 0.1
3	NbZrTiV	24.7 ± 0.2	25.4 ± 0.1	25.1 ± 0.2	24.9 ± 0.1	–

Thermal conductivity (k) was characterised by a non-contact pump-probe technique widely known as time-domain thermoreflectance (TDTR) [22–25]. In short, the output of an 80 MHz Ti:Sapphire laser is split into a pump path and a probe path. The pump path passes through an electro-optic modulator (EOM) which is modulated at the frequency of 8.4 MHz which is then detected by the probe beam and a lock-in amplifier. The probe is directed to a mechanical delay stage that enables delaying the probe with respect to the incident pump pulse and observe the changes in the thermoreflectivity of the surface with sub-picosecond temporal resolution. The polished samples were coated with 80 nm of metallic transducer, in this case aluminium, to facilitate the detection of changes in the thermoreflectivity as a result of incident pump pulses. To sample a larger area, a 10× objective lens is initially used to focus the pump and probe beams into a 13 μm spot on the coated sample surface, providing an average thermal conductivity measurement that better reflects the bulk properties of the material. For higher-resolution mapping, aimed at capturing finer variations in thermal conductivity, a 20× objective lens reduces the spot size to 4.2 μm. The sample is then scanned using a 3-axis motorized stage with a 1 μm step size, allowing detailed mapping of the thermal conductivity across the area of interest [24]. The TDTR requires the knowledge of the heat capacity (Cp) of the sample. These values were obtained by averaging the individual Cp of the pure elements [26] of the alloys. The bulk thermal conductivity was obtained by averaging 4 different scans at different sample locations and the reported uncertainty is the standard deviation of these measurements.

Nanoindentation was performed in an iMicro KLA equipment with a diamond Berkovich tip using the NanoBlitz mode for mapping areas about 250 × 250 μm in square grids with 1 μm step size and constant loads to obtain approximately 100 nm depth for the major phase (bcc1).

The evolution of yield stress (YS) with temperature was modelled on the HEAs and the bcc1 phases. The analytic model of Maresca & Curtin [27] for a strength mechanism controlled by edge dislocations in bcc-HEAs was used. It was applied using the code and data provided in the mentioned reference with a strain rate of 1×10^{-4} s^{-1}, a Taylor factor of 3.067 and a non-dimensional parameter of $\alpha = 1/12$ for the line tension calculation.

3. Results

3.1. Alloy design

The alloy design criterion applied in the present work is schematically presented in Fig. 2a. The ASAP code was used as a screening tool to assess quaternary and quinary equimolar combinations from 72 elements. Within this large number of possible alloys (≈15 million) the ASAP code was used to obtain two parameters (δ and Φ) to predict the single-phase stability at high temperatures (Fig. 2b). As explained in the introduction, values of $\Phi > 1$ and $\delta < 6.6$ predict the formation of a single-phase disordered solid-solution phase at the melting temperature [20]. This first screening reduced the possible alloys to 1664 of which 59 % are quinary combinations (Fig. 2c). The additional condition looked at in this work is a reduced macroscopic thermal neutron absorption cross-section. Therefore, we set a maximum value of $\Sigma = 0.2$ cm^{-1}, limiting the number of potential alloys to 9 (Fig. 2d). Table A.1 in the Appendix shows the potential alloys and the parameters analysed. Within this group of alloys, 3 alloys with lower Σ values and no actinide elements were selected for experimental studies in the present work (see Table 1).

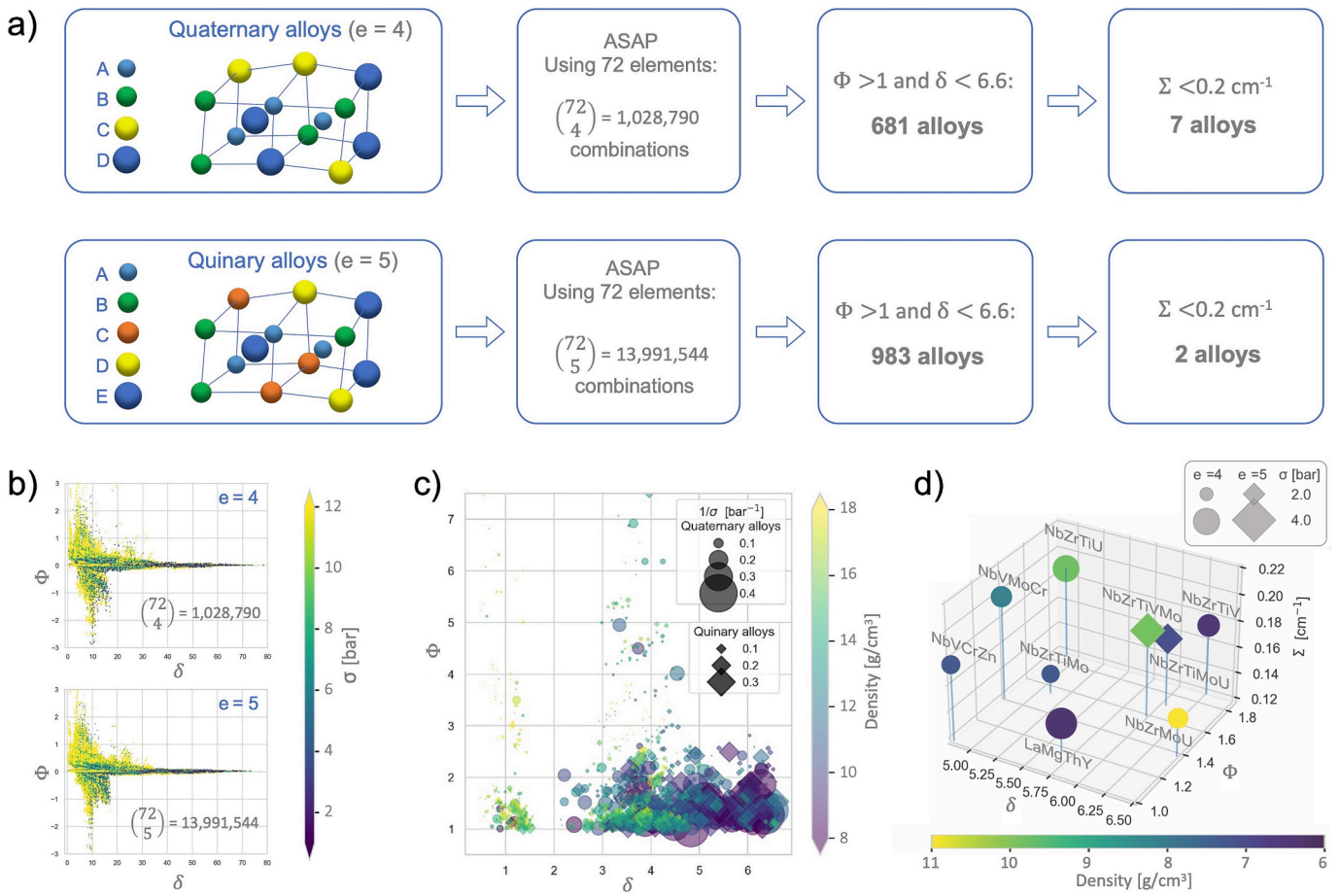

Fig. 2. Design of quaternary and quinary HEAs. a) Schematic representation of the design criterion applied. b) Φ and δ for all possible combinations. c) Alloys with the possibility of forming single-phase stability at high temperatures ($\Phi > 1$ and $\delta < 6.6$) and low microscopic thermal neutron absorption cross-section indicated by symbol size ($1/\sigma$). d) Sub-selection of alloys with the lower macroscopic thermal neutron absorption cross-section ($\Phi > 1$, $\delta < 6.6$ and $\Sigma < 0.2$ cm^{-1}).

3.2. Phase prediction and X-ray diffraction

Equilibrium molar phase fractions were calculated by the CALPHAD method. The predictions for the three selected HEAs are shown in Fig. 3. A single-phase bcc field under the solidification temperature is predicted in all the alloys. For medium temperatures, the formation of a bcc2 phase is predicted for the three alloys. In addition, at lower temperatures, the bcc2 is replaced by an hcp phase for the NbZrTiMo and NbZrTiVMo alloys. Only a 3-phase field is predicted for the quinary NbZrTiVMo alloy with a Laves C15 phase below 1000 °C. Fig. 4 shows the phases measured by XRD in the heat-treated samples. These measurements indicated two- or three-phase fields for the alloys samples treated at 1200 °C.

3.3. Phase mapping characterisation

In order to characterise the three HEAs, multiple mapping techniques were used in the alloys aged at 1200 °C. Figs. 5, 6, and 7 show the characterisation mapping in the co-located regions of interest by SEM, EBSD, EDS, TDTR, and nanoindentation, in the NbZrTiMo, NbZrTiVMo and NbZrTiV alloys respectively. The figures only show a sample region where all techniques were matched in the mapping area. Table 2 shows some of the phase properties extracted from the characterisation mappings. The values of phase fraction, hardness and elastic modulus used the full area of measurement, which are larger than the ones presented in the co-located figures. The 3 alloys have in common the formation of a primary bcc matrix phase (bcc1) and a low volume fraction of a second (bcc2) phase. A single bcc structure indexed both phases on the EBSD, therefore the bcc1 and bcc2 phases are shown in the same colour in the

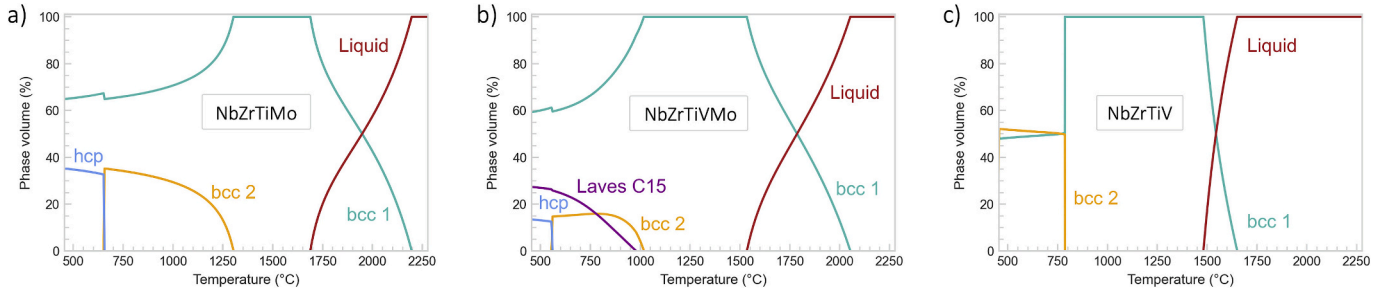

Fig. 3. Phase equilibrium modelled by Thermocalc using TCHEA6 database. a) NbZrTiMo, b) NbZrTiVMo and c) NbZrTiV.

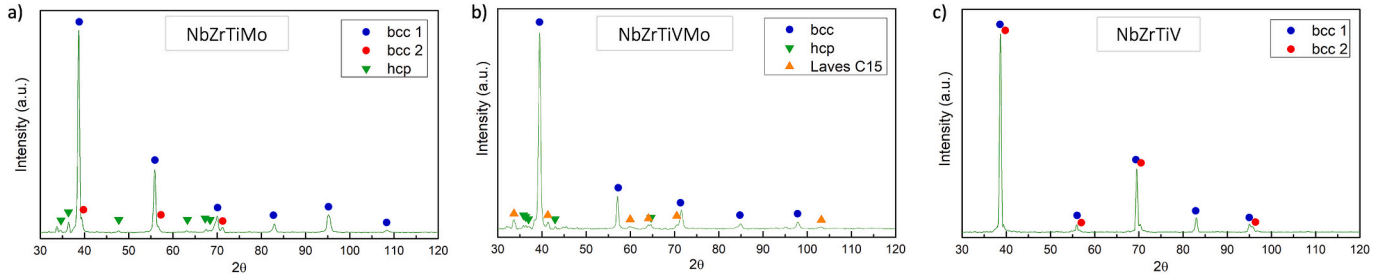

Fig. 4. Phase characterisation by XRD in a) NbZrTiMo, b) NbZrTiVMo and c) NbZrTiV, following annealing at 1200 °C.

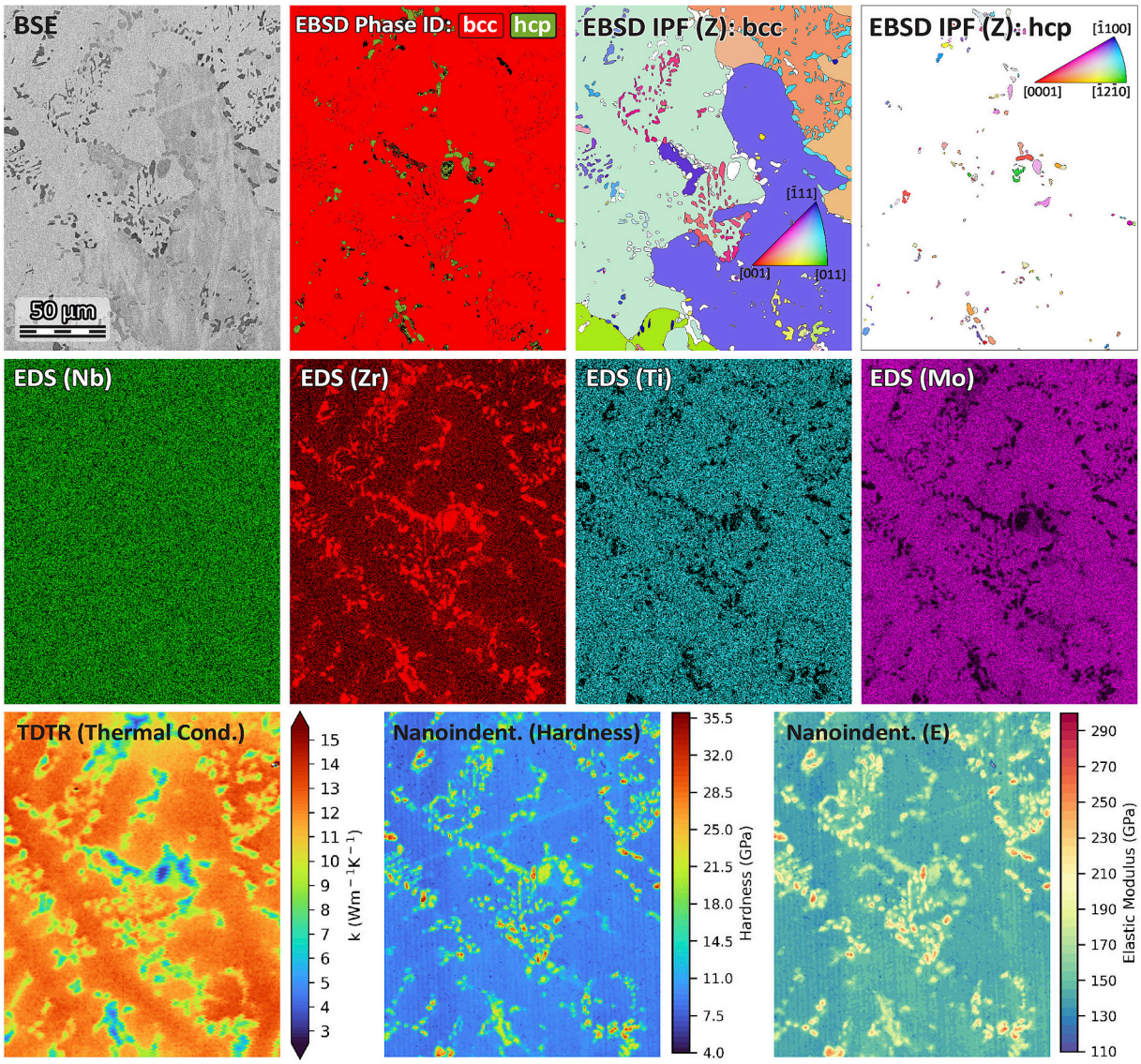

Fig. 5. NbZrTiMo alloy 1200 °C aged, mapping by: SEM (SE & BSE), EBSD (phase identification & Inverse pole figure), thermal conductivity (by TDTR), nano-indentation (hardness & elastic modulus), and EDS (elements), with scale bar common across all images.

EBSD phase identification (Phase ID) mappings. On the other hand, in the inverse pole figures (IPF), the bcc2 precipitates are distinguished by having a different orientation compared to the bcc1 matrix. In turn, observing the zirconium EDS, it is observed that the bcc2 precipitates have a high Zr content. The bcc2 precipitates have small grain sizes (<15 μm) on the three alloys which simplifies its identification with respect to the bcc1 phase. Table 2 shows the phase area fractions from EBSD analysis, and the composition of each phase obtained by averaging point-EDS measurements.

The alloy NbZrTiVMo (Fig. 6) has an hcp phase with a poor band contrast (see darker regions) which produced many incorrect indexation points. Therefore, the hcp was excluded in the EBSD indexation (Phase ID and IPF(Z) without hcp). Subsequently, the reclassification phase function in Aztec software was applied considering the band contrast (see darker regions) and pattern quality, achieving a proper identification of the 4 phases present in the alloy.

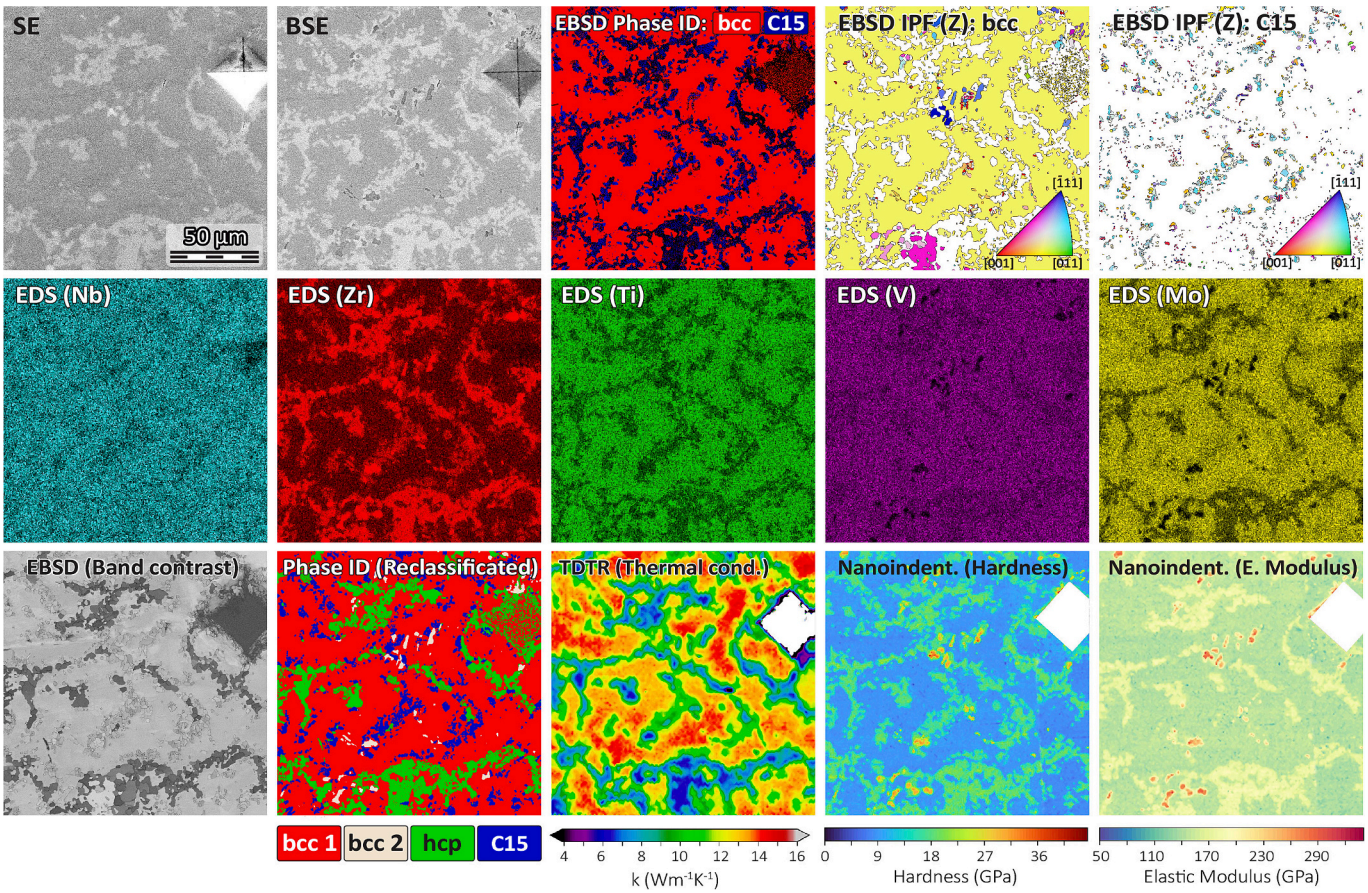

Fig. 6. NbZrTiVMo alloy 1200 °C aged, mapping by: SEM (SE & BSE), EBSD (phase identification & Inverse pole figure), thermal conductivity (by TDTR), nanoindentation (hardness & elastic modulus), and EDS (elements). There is a micro indentation in the upper right corner used for co-location (area excluded from phase property analysis), with scale bar common across all images.

The determination of the elastic modulus (E) by nanoindentation requires the Poisson's ratio (ν) of the material. Tian et al. used ab initio theory to determine the bulk properties of alloys in the Nb-Zr-Ti-V-Mo system and obtained the following ν for the equimolar alloys studied here: ν(NbZrTiMo) = 0.328, ν(NbZrTiVMo) = 0.329 and ν(NbZrTiV) = 0.330 [28]. We used the ν reported by Tian et al. to obtain the nanoindentation E maps for each alloy. The E errors shown in Table 2 have been introduced to account for the effect of approximately 10 % variation in ν. The classical method of Oliver and Pharr allows the estimation of a reduced elastic modulus (E_r), which depends on the ν and E of the material (m) and the indenter (i), as follows [29]:

$$E_r = \frac{(1-\upsilon_m^2)}{E_m} + \frac{(1-\upsilon_i^2)}{E_i} \quad (3)$$

Eq. (3) was used to estimate the E errors ($E \pm \Delta E$) in each phase for approximately 10 % variation in ν ($\nu \pm \Delta\nu_{error} = \nu \pm 0.033$), see Table 2. The indenter parameters used for these estimations were $E_i = 1140$ GPa and $\upsilon_i = 0.07$. It could be seen that an unknown ν gives a small bias ($\sim$ 2.5%) in E nanoindentation compared to experimental errors or alloy heterogeneities.

3.4. Alloys properties

Histograms of the TDTR mapping data were plotted in Fig. 8 to determine the thermal conductivity of the bcc1 phase for the three HEAs. The higher frequency peak observed in Fig. 8 corresponds to the k value of the bcc1 phase. A different k determination method was used for the additional minority phases as the spot size of the TDTR mapping is large with respect to the size of the additional phases. This introduces an intermediate k value at the interface of the matrix (bcc1) and the additional phases, which has a high frequency of occurrence in the histograms of Fig. 8. Therefore, to minimize this error, the k values were extracted from the centres of the largest particles of each phase.

For the nanoindentation mapping data, plots of hardness vs E were made to analyse the values of each phase (see Fig. 9). The higher density of points allows the extraction of hardness and E values, and for improving this determination histograms of both variables were plotted. The bcc2 phase has a small amount of data for applying this methodology. Therefore, the hardness and E values were extracted from the centres of the larger bcc2 grains. Table 2 shows the values obtained in all phases for the three alloys.

Figs. 5, 6, and 7 show the EDS composition mapping in the alloys, however, to obtain the composition of each phase (Table 2), point EDS measurements were additionally made. The average phase compositions are given in Table 2 and for comparison, these values are plotted in Fig. 10a.

The alloy's bulk properties were additionally characterised, Fig. 10b shows the alloy densities, bulk thermal conductivity, and HV1 hardness. Maresca & Curtin [27] developed an analytical model for a strength mechanism controlled by edge dislocations in bcc-HEAs. The authors presented a theory supported by experiments in bcc-HEAs indicating that strength is controlled by edge dislocations. Here, the analytical model was used to evaluate the yield stress of the three alloys with temperature. The modelling was performed for the alloys considering them as equimolar single-phase bcc. Although this is a microstructural simplification somewhat distant from reality, it is useful for future property optimization when considering a potential bcc solid solution obtained through higher-temperature treatments with respect to the

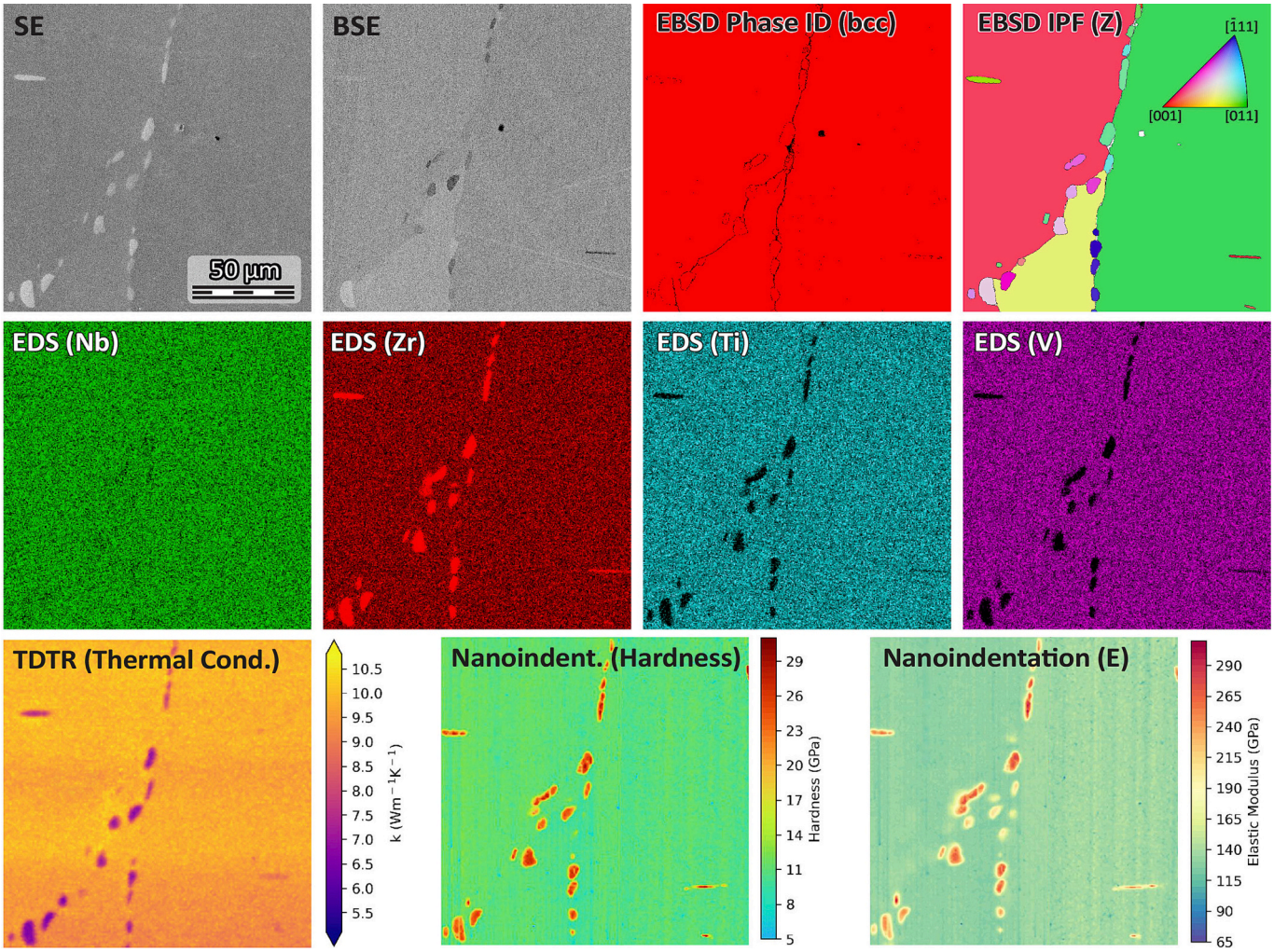

Fig. 7. NbZrTiV alloy 1200 °C aged, mapping by: SEM (SE & BSE), EBSD (phase identification & Inverse pole figure), thermal conductivity (by TDTR), nanoindentation (hardness & elastic modulus), and EDS (elements), with scale bar common across all images.

Table 2
Phase properties extracted from characterisation mappings and EDS point measurements on the alloys aged at 1200 °C. Phase area fraction (by EBSD), phase chemical composition (by EDS), thermal conductivity (k, by TDTR), and hardness and elastic modulus (E, by nanoindentation).

Alloy	Phase	Phase fraction (area. %)	Chemical composition (at.%)					$K\left(\frac{W}{m.K}\right)$	Hardness (GPa)	$E \pm \Delta E$ (GPa)
			Nb	Zr	Ti	V	Mo			
NbZrTiMo	bcc1	88.7	27.0 ± 0.5	18.8 ± 1.5	27.1 ± 0.3	–	27.1 ± 1.3	12.3	9.3	143 ± 3.6
	bcc2	9.7	3.1 ± 1.3	90.6 ± 3.2	5.8 ± 1.2	–	0.5 ± 1.0	7.1	32	271 ± 6.9
	Hcp	1.6	3.0 ± 1.1	86.1 ± 2.8	10.4 ± 1.0	–	0.5 ± 0.9	3.6	21.7	180 ± 4.6
NbZrTiVMo	bcc1	71.9	24.8 ± 0.4	10.0 ± 0.5	25.2 ± 0.4	19.8 ± 0.4	20.2 ± 0.7	13.4	8.7	145 ± 3.7
	bcc2	1.7	2.7 ± 0.7	89.5 ± 2.9	5.5 ± 0.8	1.7 ± 0.8	0.6 ± 0.8	6.3	34	285 ± 7.3
	C15	10.5	7.8 ± 0.2	49.5 ± 0.4	9.8 ± 0.2	18.3 ± 0.3	14.6 ± 0.2	9.4	17.6	147 ± 3.8
	Hcp	15.9	9.9 ± 0.3	31.3 ± 0.3	7.7 ± 0.1	26.3 ± 0.4	24.8 ± 0.2	6.2	18.5	176 ± 4.5
NbZrTiV	bcc1	98.4	24.7 ± 0.2	24.4 ± 0.1	25.7 ± 0.2	25.2 ± 0.2	–	9.8	11.3	132 ± 3.4
	bcc2	1.6	3.1 ± 1.4	90.4 ± 4.2	4.7 ± 1.2	1.8 ± 1.6	–	6.4	30	277 ± 7.1

bcc1 phase formed here. Additionally, the YS of the non-equimolar bcc1 phase (composition in Table 2) were modelled for comparison. The modelling results for temperatures between 0 and 1000 °C are shown in Fig. 10c.

4. Discussion

The HEAs examined in this study exhibit numerous similarities despite their differences in chemistry, and thus the discussion is structured as a comparative analysis of the properties of the alloys, rather than as a separate discussion for each alloy.

4.1. Alloy selection and phase prediction

After applying the modelling & design criteria of Fig. 2, here were selected two quaternary alloys (NbZrTiMo and NbZrTiV) and one quinary alloy (NbZrTiVMo) were selected for experimental studies. The selected HEAs have in common Nb, Zr, and Ti and the two quaternary alloys have V or Mo as the fourth alloying element, while the quinary alloy contains both elements (V and Mo). The HEAs here selected belong

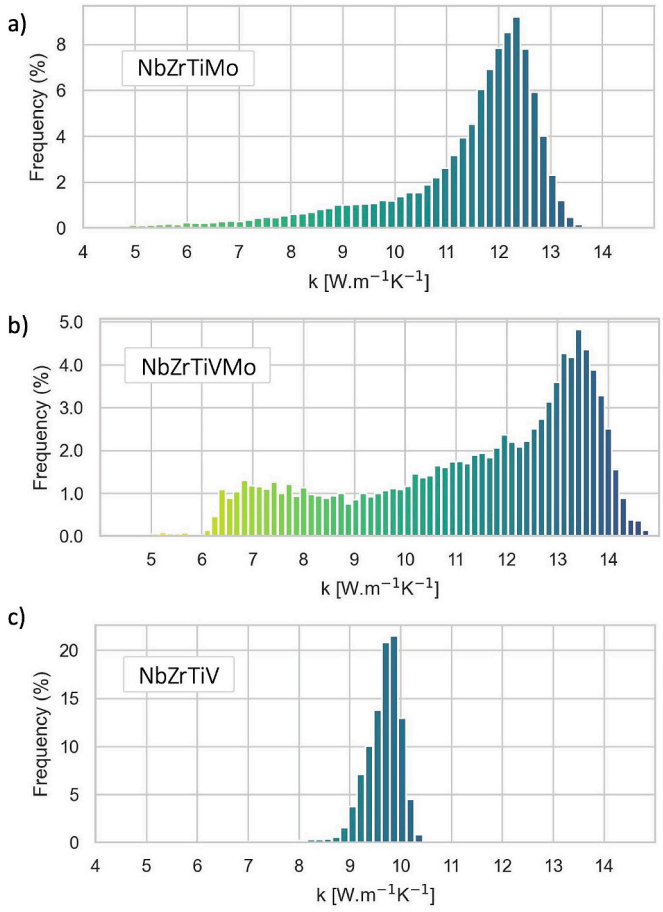

Fig. 8. Histograms of thermal conductivity from TDTR mapping. The peak containing the majority of the data corresponds to the bcc1 phase thermal conductivity. a) NbZrTiMo alloy, b) NbZrTiVMo alloy, and c) NbZrTiV alloy.

to the Nb-Zr-Ti-V-Mo system which has already captured the attention of other researchers due to: the refractory composition [30], low density [31], high degree of elastic isotropy [28], mechanical properties [32–37], and low neutron absorption cross-section [20,38].

The empirical criterion for predicting a single-phase bcc field below the solidification temperature aligns well with the phase equilibria modelled by Thermocalc (Fig. 3). Additionally, while XRD confirmed a dominant bcc phase for the three alloys in the treated condition at 1200 °C for 100 h, it also revealed additional minor phases (see Fig. 4), suggesting that higher treatment temperature, or modified compositions, might be needed to achieve a fully single-phase structure. Importantly, the presence of these secondary phases enhances our characterisation, allowing us to gain valuable insights into the individual properties of other phases within the Nb-Zr-Ti-V-Mo system, which could be used as reinforcing precipitates in onwards alloys. This additional information will support future optimization efforts as these equimolar alloys are further refined into compositionally complex alloys toward end applications.

4.2. Mapping characterisation and alloy properties

The characterisation of phases in new alloy systems becomes increasingly complex and challenging as the number of phases & alloying additions increases. Moreover, certain distinctive characteristics of each phase may only be detectable in specific properties, which can limit the effectiveness of individual characterisation techniques in distinguishing between phases. To mitigate this issue, integrating multiple characterisation techniques within the same sample region can enhance the accuracy and confidence in identifying and analysing the phases present in a previously unknown alloy. In this study, we combined electron microscopy, TDTR, and nanoindentation for mapping the same sample region on the three selected HEAs. These mappings are shown in Figs. 5, 6, and 7, this approach allowed us to extract detailed phase characteristics, including phase identification, size, morphology, distribution, phase fraction, crystal orientation, chemical composition, thermal conductivity, hardness (with consideration of the indentation size effect), and *E*.

4.2.1. Phase formation

The careful melting strategy of the alloys successfully avoided macrosegregation in the ingot as is reflected by the reduced standard deviation of the elements along the ingot (see Table 1), which is often a challenge when producing RHEAs. The three alloys formed a majoritarian bcc (bcc1) phase with phase area fractions of 88.7 %, 71.9 % and 98.4 % for NbZrTiMo, NbZrTiVMo, and NbZrTiV, respectively. The bcc1 is closer to the equimolar composition but depleted in Zr in all the alloys, as can be seen in Fig. 10a. On the contrary, all the additional phases are rich in Zr. The tendency of Zr to promote the formation of additional intermetallic compounds in HEAs, due to the negative and very low mixing enthalpy between Zr and other metals, which was observed in previous works [31,39]. The second phase, which was observed in all alloys, was an additional bcc (bcc2) with a composition rich in Zr (approximately 90 at.%). The phase area fraction was 9.7 % for the NbZrTiMo alloy and less than 2 % for the other two alloys. In the NbZrTiMo alloy, the bcc2 is present in a dispersed state within the bcc1-matrix, and in groups of precipitates with equal orientation indicating a colony growth formation. These bcc2 colonies are interconnected and likely formed through interdendritic solidification. In contrast, the other quaternary NbZrTiV alloy showed the bcc2 to be localized primarily on bcc1-matrix grain boundaries.

A hcp phase was found in the NbZrTiMo and NbZrTiVMo alloys. Even though these two alloys share a common Mo constituent, this does not appear to be the underlying cause for the formation of this phase, since the Mo content in the hcp phase is essentially negligible in the quaternary alloy. A comparison of the compositions of the hcp phases in the two alloys reveals no apparent similarities, except for Zr, which is present in significantly higher concentrations in both. In the NbZrTiMo alloy, the bcc2 and hcp have similar compositions, in agreement with Thermocalc modelling, which predicts the transformation of bcc2 to hcp at lower temperatures. Both phases show similar distributions and sizes, which may indicate that the transformation process from bcc2 to hcp was only partially completed during the heat treatment.

Finally, the quinary alloy was the only alloy to form a Laves C15 phase. Thermocalc predicted the Laves C15 in the NbZrTiVMo alloy, but for temperatures below 1000 °C. A 10.5 % Laves C15 phase area fraction was observed with around 50 %at Zr content. Similarly, Wu et al. reported a Laves C15 rich in Zr, V and Mo with depletion of Nb and Ti in the $NbZrTiV_{0.3}Mo_{0.7}$ alloy [35], while Wang et al. [40] reported Laves C15 phase formed at grain boundaries in an as-cast NbZrTiV alloy.

4.2.2. Thermal conductivity

The severe lattice distortion and extensive atomic occupational disorder in HEAs result in strong phonon scattering and low electron and phonon conductivity [41,42]. Therefore, HEAs typically exhibit low thermal conductivity making them promising as irradiation resistance materials [21,43]. The higher irradiation resistance is attributed to the increase of point defect recombination due to a thermal spike that is more localized and with a longer duration, as well as a broadening of interstitial and vacancy migration energy distributions [44,45]. However, in certain applications low thermal conductivity can become an issue where high heat flow through a component is required.

The overall room temperature thermal conductivities measured in the present work are typical to the low values generally observed in HEAs [46–48]. Nevertheless, the mapping characterisation of the

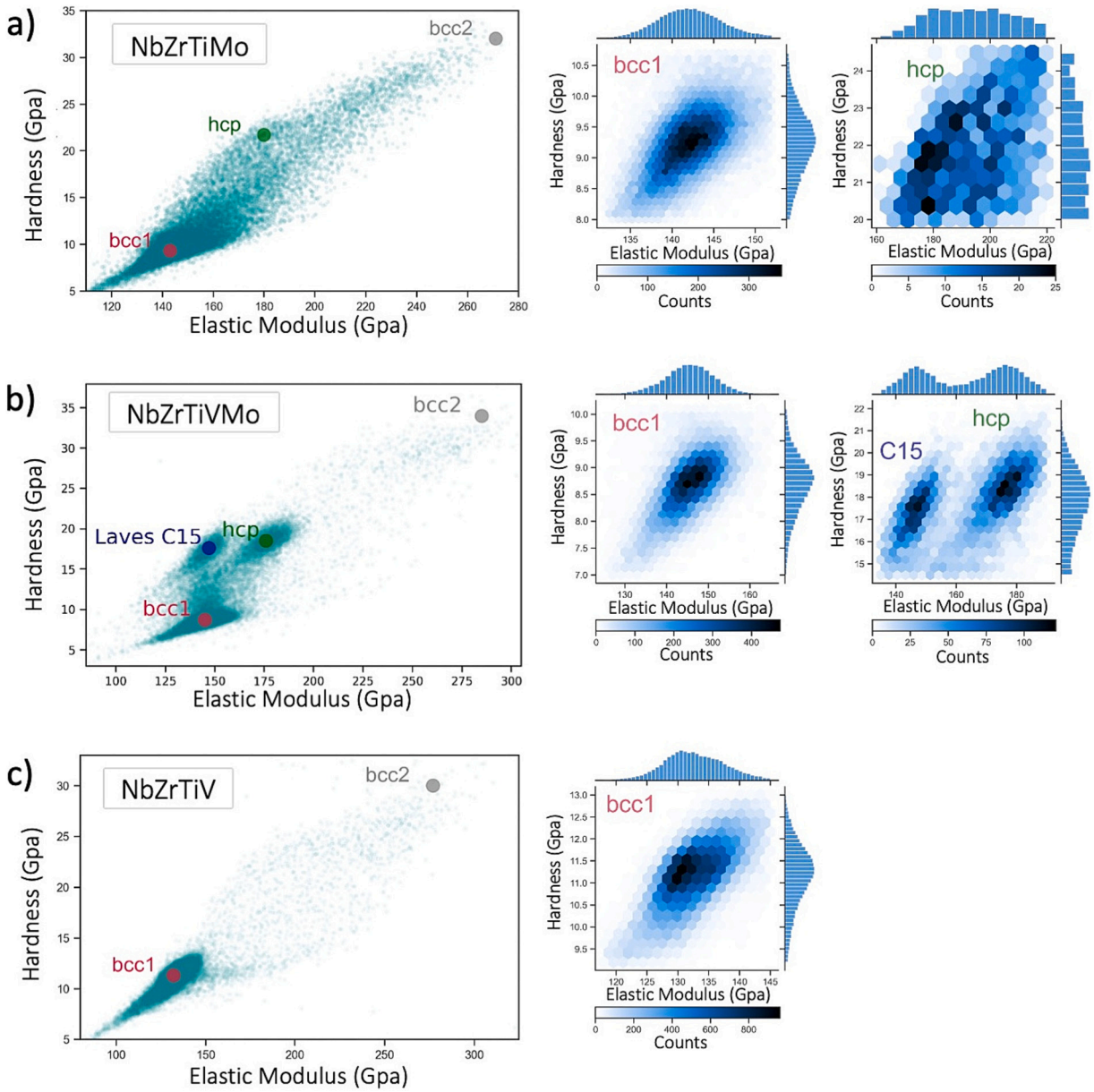

Fig. 9. Hardness versus *E* and histograms extracted from the nanoindentation mapping. a) NbZrTiMo alloy, b) NbZrTiVMo alloy, and c) NbZrTiV alloy.

thermal conductivity across the multiple phases that these HEAs have formed provides a basis for guiding the optimisation of bulk alloy thermal conductivity particularly from the perspective of secondary-phase reinforcement.

The highest thermal conductivity values were observed in the bcc1 (matrix) phase for the three alloys, as evidenced by the thermal conductivity mappings (Figs. 5, 6, and 7). This phase is of the highest relevance, both in terms of its phase percentage and its proximity to the equimolar composition. The bcc1 with Mo content, NbZrTiMo and NbZrTiVMo alloys, exhibit higher thermal conductivities than the bcc1 phase in the NbZrTiV alloy, as shown in Table 1. Conversely, the bcc2 phase exhibits considerably lower *k* values, which can be attributed to its Zr-rich composition, since Zr has a relatively low k value when present as a pure element. The hcp exhibited a similar trend, displaying higher k values in the quinary alloy than in the quaternary alloy which has a negligible amount of Mo. As expected, Fig. 10b illustrates the bulk thermal conductivities that are close to, but lower than, the respective bcc1 phase values. The collected evidence indicates that the suppression of additional phases and the increase of Mo content will result in higher bulk thermal conductivity. Optimising the thermal conductivity will offer advantages in designing the geometry of ATF cladding and further atomistic modelling is required to understand the role of thermal conductivity on cascade morphology in these alloys.

4.2.3. *Hardness, elastic modulus and density*

Hardness values obtained by nanoindentation are subject to overestimation due to the indentation size effect [49]. However, nanoindentation enables the acquisition of independent hardness for the small-sized phases present in the regions mapped here.

Table 2 shows the nanoindentation hardness measurements, with values around 9 GPa on the bcc1 phase for NbZrTiMo and NbZrTiVMo alloys, and 11 GPa for the NbZrTiV alloy. On the other hand, the *E* of the bcc1 phase showed higher values in the two Mo-containing alloys (~144 GPa) and a lower value in the NbZrTiV alloy (132 GPa). Considering that the bcc1 phases are close to the nominal equimolar compositions, it is possible to compare these values with the ab initio *E* obtained by Tian et al. [28] on the same 3 equimolar alloys. The reported ab initio *E* values are about 141 GPa for the two Mo-containing

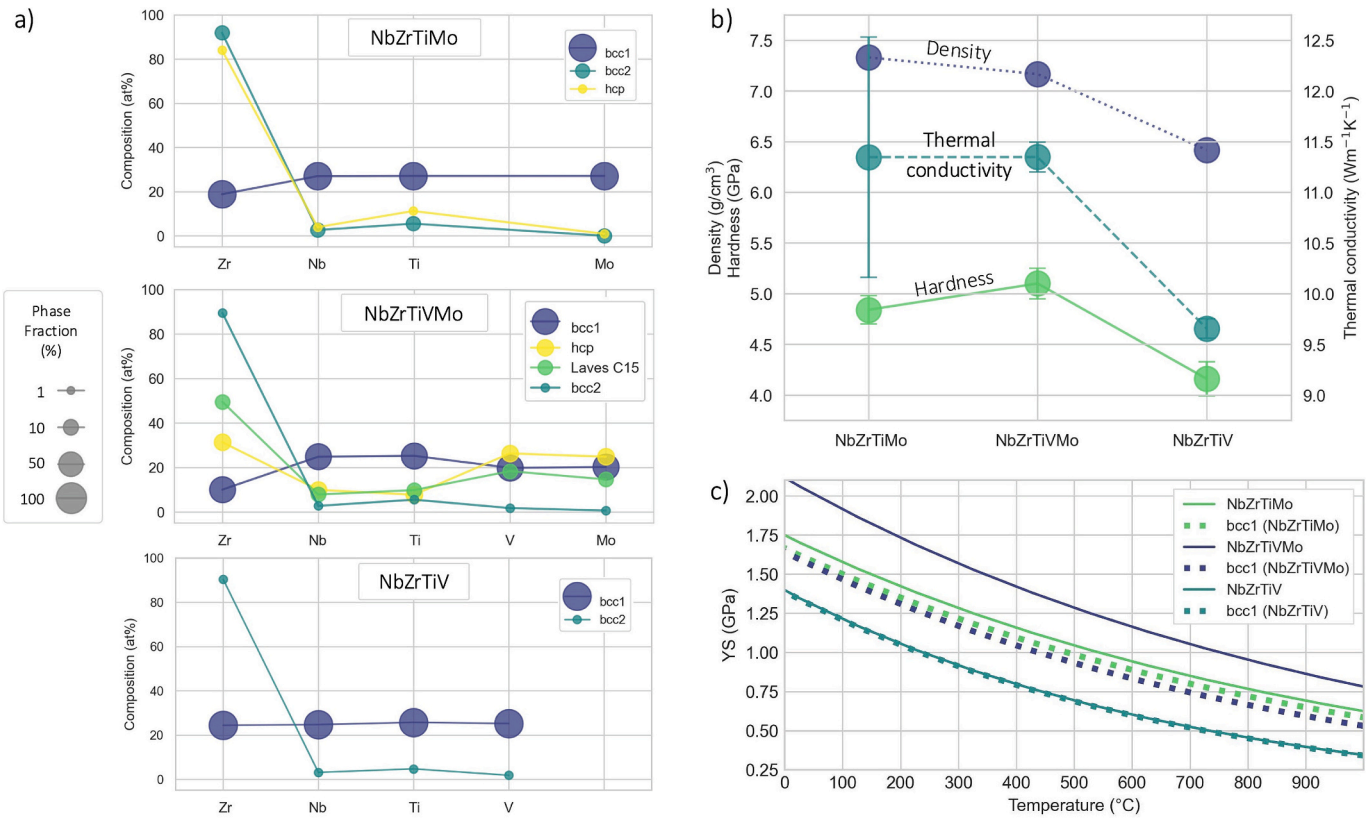

Fig. 10. Alloys properties: a) EDS phase composition from point measurements. b) Alloy density, thermal conductivity, and hardness HV1. c) Modelling of YS vs temperature for the equimolar HEAs and the bcc1 phase (see composition in Table 2).

alloys and 121 GPa for the NbZrTiV alloy, showing the same trend and remarkably close to those measured here experimentally. Similar ab initio results, although about 3 GPa lower, were later obtained on the same equimolar alloys by Tian et al. [37].

Similar hardness values were found for the Zr-rich bcc2 on the three alloys, but in this case the values were much higher than the bcc1, above 30 GPa. The *E* of bcc2 ranged from 271 GPa to 285 GPa for the alloys, which is about twice the bcc1 *E*.

The remaining phases, hcp and Laves C15, exhibited hardness and *E* values intermediate between bcc1 and bcc2, although closer to bcc1 as shown in Fig. 9. Interestingly, Fig. 9b shows that the quinary alloy has similar hardnesses in the Laves C15 and hcp phases, and similar *E* in the Laves C15 and bcc1 phases. These pairs of similar phase properties generate a mimicry between the phases, which could lead to erroneous conclusions if instead of multiple characterisation techniques a single property is observed. The effect of phase mimicry can be seen in the nanoindentation mappings in Fig. 6 for the hardness (Laves C15 and hcp) and *E* (Laves C15 and bcc1). The same pair of phase mimicry is found in the BSE and SE mappings.

It should be noted that nano-hardness is overestimated due to indentation size effects (ISE), which increase with shallower indents (e.g., on the bcc2 phase). The degree of ISE affecting the nano-hardness can be roughly estimated, for example, in the NbZrTiV alloy, in which second phases are negligible. This can be seen by comparing the bulk hardness value (4.2 GPa, Fig. 10b) with the hardness obtained by nanoindentation in the bcc1 phase (11.3 GPa, Table 2).

Fig. 10b shows the bulk hardness of the alloys with the higher value of 5.1 GPa for the NbZrTiVMo alloy, followed by 4.8 GPa for the NbZrTiMo alloy and 4.2 GPa for the NbZrTiV alloy. The same relationship trend between the alloys at room temperature is reflected in the modelling of the YS alloys in Fig. 10c. The figure also shows the decrease in YS with increasing temperature, which is similar for the three HEAs, and therefore the trend between them does not change at higher temperatures. In contrast, when comparing the bcc1 YS, the modelling of Fig. 10b shows that the bcc1 in NbZrTiMo has a slightly higher value than the bcc1 of the NbZrTiVMo alloy, and below is the bcc1 of the NbZrTiV alloy, which agrees with the nanoindentation hardness measurements (see Table 2). It is interesting to note the marked decrease in YS of the bcc1 (non-equimolar) with respect to the equimolar NbZrTiVMo alloy.

Given this evidence and the fact that YS can be estimated as proportional to hardness, it can be concluded that the bulk alloy hardness and YS on these HEAs have two opposite effects when additional phases are formed: Hardness and YS increase with the addition of high-hardness phases, but decrease with element depletion within the bcc1. In the quinary alloy, these effects are more pronounced because it has a greater tendency to form additional phases.

The density measured in the alloys is displayed in Fig. 10b. The NbZrTiV alloy has the lower density (6.42 g/cm^3) which makes it more interesting as a nuclear structural material. This lower density value is slightly lower than Zircaloy-4 (6.56 g/cm^3), as other authors have previously noted [20].

4.3. Relevance of the alloys for nuclear applications

The solidus temperature (ST) is an important parameter that reflects an upper potential of alloys to be used at high temperatures. The three equimolar alloys can be ranked by ST using Thermocalc in the following order: NbZrTiMo (ST = 1697 °C), NbZrTiVMo (ST = 1537 °C), and NbZrTiV (ST = 1482 °C).

A single bcc phase microstructure could be achieved at higher temperatures than 1200 °C in the two alloys with Mo, and/or by modifying the composition. However, it will be unfeasible for use it as a single-phase bcc alloy at intermediate temperatures, because the multiphase equilibrium will be reached in short time frames. In contrast, although the NbZrTiV alloy showed a bcc2 phase at grain boundaries for the

1200 °C treatment, the amount of bcc2 was very small and not observed in previous work [20]. Therefore, disregarding the bcc2 phase and considering the results of King et al. [20], the NbZrTiV alloy could be considered as a single bcc phase alloy for a wider range of applications. According to the phase equilibrium modelled by Thermocalc (Fig. 3c) the bcc solid solution range extends from 787 °C up to ST = 1482 °C. On their other hand, the multi-phase found in these alloys could be used in the future has a nanoscale reinforcement strategy handled by precipitation treatments.

The Zr-based alloys commonly used as cladding in fission reactors have an exceptionally low macroscopic neutron absorption cross-section, which quaternary or quinary equimolar HEAs will never achieve. Therefore, in this aspect equimolar HEAs are not competitive with Zr-base alloys. However, in nuclear applications such as fast reactors or advanced sodium/lead reactors where steels are used or considered [50,51], HEAs may be superior, particularly for their added strength and radiation resistance. Table 3 illustrates this with alloys ranked from lower to higher macroscopic thermal neutron absorption cross-section. Although far behind Zircaloy-4 (close to pure Zr), the NbZrTiMo alloy has the smallest value among the quaternary and quinary RHEAs and is about the half value of many commercial steels.

Recently, Zhang et al. explored the irradiation damage in non-equimolar HEAs of the Ti–Zr–Nb–V–Mo system and proposed it as an accident-tolerant fuel cladding material [38]. They found low irradiation hardening levels, and a decrease in the growth of He bubbles with an increase in the component number, and comprehensive mechanical properties at RT and elevated temperatures. From Zhang's perspective, our quinary alloy is the most promising from the three alloys studied here. In order to determine the optimal heat treatments and microstructure, it is essential to ascertain the extent to which the irradiation damage resistance can be enhanced by the presence of secondary phases. Two mechanisms may contribute to enhancing irradiation damage resistance by secondary phases. The first is the formation of phase interfaces that act as sink sources for radiation defects, assisting the recombination of interstitials and vacancies [52–54]. The second is the low thermal conductivity, which was previously discussed in Section 4.2.2. The present study demonstrated that the incorporation of additional phases markedly reduces the thermal conductivity in HEAs, particularly in the two Mo-containing alloys. These findings offer valuable insights into the complex mechanisms governing irradiation damage resistance in HEAs.

Some refractory bcc-HEAs can hold high strength at higher temperatures even exceeding some Ni-base superalloys [55,56]. This effect is attributed to a dominant edge-dislocation plastic flow prevalent up to high temperatures. If the same dislocation behaviour is maintained at elevated temperatures in the studied alloys, the quinary NbZrTiVMo alloy will exhibit the YS of approximately 750 MPa at 1000 °C, as indicated by the modelling presented in Fig. 10c. Conversely, the high-entropy alloy without Mo (NbZrTiV) displays an YS that is approximately half that of the NbZrTiVMo alloy at these elevated temperatures.

5. Conclusions

This work establishes an integrated phase-mapping strategy that combines SEM/EDS/EBSD, nanoindentation, and time-domain thermoreflectance (TDTR) to correlate microstructural, thermal, and mechanical properties in equimolar refractory HEAs designed for reduced thermal neutron cross-sections and single-phase stability at high temperature. Out of ~15 million quaternary and quinary compositions screened, three promising alloys, NbZrTiMo, NbZrTiVMo and NbZrTiV were experimentally investigated. All exhibited a majority bcc matrix with secondary Zr-rich phases following treatment at 1200 °C for 100 h. The multi-technique approach provided complementary resolution that no single method could achieve. Key findings are highlighted as below:

Table 3
Microscopic and macroscopic thermal neutron absorption cross-section (σ and Σ, respectively) of nuclear application alloys. Impurities and low-content elements were excluded from the calculation (see compositions and densities in Appendix Table A.2).

Alloy	σ [barns]	Σ [cm^{-1}]
Zircaloy-4	0.198	0.0085
NbZrTiMo	2.476	0.1331
NbZrTiVMo	2.997	0.1698
NbZrTiV	3.126	0.1722
75Fe20Cr5Al [51]	2.433	0.1977
P92	2.643	0.2222
316 SS	2.987	0.2501
304 SS	3.011	0.2530
310 SS	3.216	0.2717

- The equimolar-like bcc1 matrix dominates alloy behaviour, with thermal conductivity values up to ~12 $W{\cdot}m^{-1}{\cdot}K^{-1}$ and nanohardness around 9–11 GPa.
- Mo additions stabilize the bcc1 matrix and enhance bulk thermal conductivity, while excess Zr promotes the formation of intermetallic phases (hcp, Laves C15).
- Zr-rich secondary bcc2 phases show drastically high nanohardness (>30 GPa) and elastic modulus, higher than hcp and Laves C15 phases. Thus, it could be used as an efficient strengthening semi-coherent phase instead of hcp or Laves C15 phases. The bcc2 phase can impact the thermal conductivity of alloys due to its low value (~6 $W{\cdot}m^{-1}{\cdot}K^{-1}$).
- Bulk hardness (HV1) values ranged from 4.2 GPa (NbZrTiV) to 5.1 GPa (NbZrTiVMo), consistent with yield strength predictions from dislocation-based modelling, offering an effective way to predict the macroscopic strength of the screened alloys.

Overall, these results provide compositional guidelines, suppressing Zr-rich phases while increasing Mo, and a methodological advance for designing new alloys. The correlative mapping approach strengthens confidence in phase identification and accelerates the design for targeting thermal-mechanical properties.

CRediT authorship contribution statement

P.A. Ferreirós: Writing – review & editing, Writing – original draft, Validation, Methodology, Investigation, Formal analysis, Conceptualization. **K. Ma:** Writing – review & editing, Validation, Investigation. **C. Bearcroft:** Validation, Investigation, Data curation. **A.J. Cackett:** Writing – review & editing. **K. Aryana:** Writing – review & editing, Resources, Methodology, Investigation. **M.S.B. Hoque:** Resources, Methodology, Investigation. **P.E. Hopkins:** Writing – review & editing, Supervision, Resources, Funding acquisition. **A.J. London:** Writing – review & editing, Supervision, Resources, Funding acquisition. **A.J. Knowles:** Writing – review & editing, Supervision, Project administration, Funding acquisition, Conceptualization.

Declaration of competing interest

The authors declare that they have no known competing financial interests or personal relationships that could have appeared to influence the work reported in this paper.

Acknowledgments

P.A. Ferreirós & A.J. Knowles acknowledge funding from the UK Engineering and Physical Sciences Research Council (EPSRC) Grant EP/T01220X/1. P.A. Ferreirós acknowledges support from the European Union Horizon 2020 research and innovation program under grant agreement no. 857470. A.J. Knowles gratefully acknowledges funding

from a UKRI Future Leaders Fellowship (MR/T019174/1 & MR/Y034155/1) and Royal Academy of Engineering Research Fellowship, UK (RF\201819\18\158). K. Ma and A.J. Knowles acknowledge funding from EU H2020 grant no. 958418 "COMPASsCO2". The authors gratefully acknowledge the Centre for Electron Microscopy (University of Birmingham) for their support & assistance in this work. The research used UKAEA's Materials Research Facility, which has been funded by and is part of the UK's National Nuclear User Facility and Henry Royce Institute for Advanced Materials. The work at UVA was supported by the Office of Naval Research, Grant No. N00014-21-1-2477. The authors would like to express their gratitude to Dr. Iael Perez for her invaluable assistance in creating figures by Python.

Appendix A

Table A.1
Alloys obtained with the design criteria presented in Fig. 3a. Empirical parameters for predicting single-phase stability at high temperatures (δ and Φ), density, microscopic and macroscopic thermal neutron absorption cross-section (σ and Σ, respectively).

Selected alloy #	Alloy	δ	Φ	Density [g/cm^3]	σ [barns]	Σ [cm^{-1}]
1	NbZrTiMo	5.12	1.53	7.32	2.48	0.133
–	LaMgThY	5.67	1.15	6.35	4.42	0.140
–	MoNbUZr	6.50	1.36	11.07	2.85	0.147
2	NbZrTiVMo	6.06	1.69	7.13	3.00	0.170
3	NbZrTiV	6.27	1.86	6.47	3.13	0.172
–	CrNbVZn	4.83	1.00	7.33	2.60	0.176
–	MoNbTiUZr	6.00	1.57	9.87	3.50	0.184
–	NbTiUZr	4.92	1.84	9.81	3.75	0.188
–	CrMoNbV	4.83	1.39	8.14	2.94	0.197

Table A.2
Alloy densities and compositions in at.% used for the calculation of thermal neutron absorption cross-section of Table 3. Impurities and low-content elements were excluded from the calculation.

Alloy	Density [g/cm^3]	Al	Cr	Fe	Mn	Mo	Nb	Ni	Si	Sn	Ti	V	Zr
Zircaloy-4	6.525	–	0.0010	0.0015	–	–	–	–	–	0.0150	–	–	0.9825
NbZrTiMo	7.320	–	–	–	–	0.25	0.25	–	–	–	0.25	–	0.25
NbZrTiVMo	7.130	–	–	–	–	0.20	0.20	–	–	–	0.20	0.20	0.20
NbZrTiV	6.469	–	–	–	–	–	0.25	–	–	–	0.25	0.25	0.25
75Fe20Cr5Al	7.053	0.0969	0.2011	0.7021	–	–	–	–	–	–	–	–	–
P92	7.732	–	0.0958	0.8889	0.0050	0.0026	–	–	0.0077	–	–	–	–
316 SS	7.725	–	0.1869	0.6604	0.0152	0.0133	–	0.1088	0.0154	–	–	–	–
304 SS	7.663	–	0.2007	0.6761	0.0200	–	–	0.0889	0.0143	–	–	–	–
310 SS	7.715	–	0.2665	0.5177	0.0190	0.0007	–	0.1827	0.0133	–	–	–	–

Appendix B. Supplementary data

Supplementary data to this article can be found online at https://doi.org/10.1016/j.matchar.2025.115529.

Data availability

Data will be made available on request.

References

[1] B. Cantor, I.T.H. Chang, P. Knight, A.J.B. Vincent, Microstructural development in equiatomic multicomponent alloys, Mater. Sci. Eng. A 375–377 (2004) 213–218, https://doi.org/10.1016/j.msea.2003.10.257.
[2] J.-W. Yeh, S.-K. Chen, S.-J. Lin, J.-Y. Gan, T.-S. Chin, T.-T. Shun, C.-H. Tsau, S.-Y. Chang, Nanostructured high-entropy alloys with multiple principal elements: novel alloy design concepts and outcomes, Adv. Eng. Mater. 6 (2004) 299–303, https://doi.org/10.1002/adem.200300567.
[3] D. Li, P.K. Liaw, L. Xie, Y. Zhang, W. Wang, Advanced high-entropy alloys breaking the property limits of current materials, J. Mater. Sci. Technol. 186 (2024) 219–230, https://doi.org/10.1016/j.jmst.2023.12.006.
[4] N.F. Lone, F. Czerwinski, D. Chen, Present challenges in development of lightweight high entropy alloys: a review, Appl. Mater. Today 39 (2024) 102296, https://doi.org/10.1016/j.apmt.2024.102296.
[5] S. Kumar, Comprehensive review on high entropy alloy-based coating, Surf. Coat. Technol. 477 (2024) 130327, https://doi.org/10.1016/j.surfcoat.2023.130327.
[6] T. Wang, W. Jiang, X. Wang, B. Jiang, Y. Wang, X. Wang, H. Xu, M. Hu, D. Zhu, Enhanced mechanical properties of lightweight refractory high-entropy alloys at elevated temperatures via Si addition, Mater. Charact. 218 (2024) 114552, https://doi.org/10.1016/j.matchar.2024.114552.
[7] S.J. Zinkle, G.S. Was, Materials challenges in nuclear energy, Acta Mater. 61 (2013) 735–758, https://doi.org/10.1016/j.actamat.2012.11.004.
[8] Z. Zhang, D.E.J. Armstrong, P.S. Grant, The effects of irradiation on CrMnFeCoNi high-entropy alloy and its derivatives, Prog. Mater. Sci. 123 (2022) 100807, https://doi.org/10.1016/j.pmatsci.2021.100807.
[9] A. Hussain, R.S. Dhaka, H.J. Ryu, S.K. Sharma, P.K. Kulriya, A critical review on temperature dependent irradiation response of high entropy alloys, J. Alloys Compd. 948 (2023) 169624, https://doi.org/10.1016/j.jallcom.2023.169624.
[10] M.A. Khan, J. Brechtl, High-entropy alloys as an irradiation-resistant material: a review, in: High-Entropy Alloys, Elsevier, 2024, pp. 323–374, https://doi.org/10.1016/B978-0-443-22142-2.00014-4.
[11] S. Yagnik, A. Garde, Chapter 7 - zirconium alloys for LWR fuel cladding and core internals, in: G.R. Odette, S.J. Zinkle (Eds.), Structural Alloys for Nuclear Energy Applications, Elsevier, Boston, 2019, pp. 247–291, https://doi.org/10.1016/B978-0-12-397046-6.00007-1.
[12] S.J. Zinkle, K.A. Terrani, J.C. Gehin, L.J. Ott, L.L. Snead, Accident tolerant fuels for LWRs: a perspective, J. Nucl. Mater. 448 (2014) 374–379, https://doi.org/10.1016/j.jnucmat.2013.12.005.
[13] W. Li, D. Xie, D. Li, Y. Zhang, Y. Gao, P.K. Liaw, Mechanical behavior of high-entropy alloys, Prog. Mater. Sci. 118 (2021) 100777, https://doi.org/10.1016/j.pmatsci.2021.100777.

[14] D.J.M. King, S.C. Middleburgh, A.G. McGregor, M.B. Cortie, Predicting the formation and stability of single phase high-entropy alloys, Acta Mater. 104 (2016) 172–179, https://doi.org/10.1016/j.actamat.2015.11.040.
[15] X. Yang, Y. Zhang, Prediction of high-entropy stabilized solid-solution in multi-component alloys, Mater. Chem. Phys. 132 (2012) 233–238, https://doi.org/10.1016/j.matchemphys.2011.11.021.
[16] J. Gong, Y. Li, S. Liang, W. Lu, Y. Wang, Z. Chen, Efficient alloy design strategy for fast searching for high-entropy alloys with desired mechanical properties, Mater. Des. 245 (2024) 113260, https://doi.org/10.1016/j.matdes.2024.113260.
[17] J. He, Z. Li, J. Lin, P. Zhao, H. Zhang, F. Zhang, L. Wang, X. Cheng, Machine learning-assisted design of refractory high-entropy alloys with targeted yield strength and fracture strain, Mater. Des. 246 (2024) 113326, https://doi.org/10.1016/j.matdes.2024.113326.
[18] J.-C. Ren, J. Zhou, C.J. Butch, Z. Ding, S. Li, Y. Zhao, W. Liu, Predicting single-phase solid solutions in as-sputtered high entropy alloys: high-throughput screening with machine-learning model, J. Mater. Sci. Technol. 138 (2023) 70–79, https://doi.org/10.1016/j.jmst.2022.07.059.
[19] D.J.M. King, Alloy_Search_and_Predict_1.0, GitHub, 2021. https://github.com/GM-King/Alloy_Search_and_Predict_1.0.
[20] D.J.M. King, S.T.Y. Cheung, S.A. Humphry-Baker, C. Parkin, A. Couet, M.B. Cortie, G.R. Lumpkin, S.C. Middleburgh, A.J. Knowles, High temperature, low neutron cross-section high-entropy alloys in the Nb-Ti-V-Zr system, Acta Mater. 166 (2019) 435–446, https://doi.org/10.1016/j.actamat.2019.01.006.
[21] M. Caro, L.K. Béland, G.D. Samolyuk, R.E. Stoller, A. Caro, Lattice thermal conductivity of multi-component alloys, J. Alloys Compd. 648 (2015) 408–413, https://doi.org/10.1016/j.jallcom.2015.06.035.
[22] D.G. Cahill, Analysis of heat flow in layered structures for time-domain thermoreflectance, Rev. Sci. Instrum. 75 (2004) 5119–5122, https://doi.org/10.1063/1.1819431.
[23] P.E. Hopkins, J.R. Serrano, L.M. Phinney, S.P. Kearney, T.W. Grasser, C.T. Harris, Criteria for cross-plane dominated thermal transport in multilayer thin film systems during modulated laser heating, J. Heat Transf. 132 (2010) 081302, https://doi.org/10.1115/1.4000993.
[24] D.H. Olson, J.A. Deijkers, K. Quiambao-Tomko, J.T. Gaskins, B.T. Richards, E. J. Opila, P.E. Hopkins, H.N.G. Wadley, Evolution of microstructure and thermal conductivity of multifunctional environmental barrier coating systems, Mater. Today Phys. 17 (2021) 100304, https://doi.org/10.1016/j.mtphys.2020.100304.
[25] A.J. Schmidt, X. Chen, G. Chen, Pulse accumulation, radial heat conduction, and anisotropic thermal conductivity in pump-probe transient thermoreflectance, Rev. Sci. Instrum. 79 (2008) 114902, https://doi.org/10.1063/1.3006335.
[26] M.W. Chase Jr., NIST-JANAF thermochemical tables, Monograph 9, 4th ed. J. Phys. Chem. Ref. Data (1998) 1577–1944.
[27] F. Maresca, W.A. Curtin, Mechanistic origin of high strength in refractory BCC high entropy alloys up to 1900K, Acta Mater. 182 (2020) 235–249, https://doi.org/10.1016/j.actamat.2019.10.015.
[28] F. Tian, L.K. Varga, N. Chen, J. Shen, L. Vitos, Ab initio design of elastically isotropic TiZrNbMoV high-entropy alloys, J. Alloys Compd. 599 (2014) 19–25, https://doi.org/10.1016/j.jallcom.2014.01.237.
[29] W.C. Oliver, G.M. Pharr, An improved technique for determining hardness and elastic modulus using load and displacement sensing indentation experiments, J. Mater. Res. 7 (1992) 1564–1583, https://doi.org/10.1557/JMR.1992.1564.
[30] Z. Leong, U. Ramamurty, T.L. Tan, Microstructural and compositional design principles for Mo-V-Nb-Ti-Zr multi-principal element alloys: a high-throughput first-principles study, Acta Mater. 213 (2021) 116958, https://doi.org/10.1016/j.actamat.2021.116958.
[31] P. Zhang, D. Sun, S.A. Ibrahim, Z. Su, T. Shi, Y. Li, X. Qiu, C. Lu, Influence of multiphase microstructure on the strength and ductility of Nb–Zr–Ti–V refractory high entropy alloys, Mater. Sci. Eng. A 912 (2024) 146954, https://doi.org/10.1016/j.msea.2024.146954.
[32] Y. Chen, X. Gao, G. Qin, R. Chen, J. Guo, Achieving excellent specific yield strength in non-equiatomic TiNbZrVMo high entropy alloy via metalloid Si doping, Mater. Lett. 335 (2023) 133832, https://doi.org/10.1016/j.matlet.2023.133832.
[33] F. Zhang, C. Xiang, E.-H. Han, Z. Zhang, Effect of Nb content on microstructure and mechanical properties of Mo0.25V0.25Ti1.5Zr0.5Nbx high-entropy alloys, Acta Metall. Sin. (Engl. Lett.) 35 (2022) 1641–1652, https://doi.org/10.1007/s40195-022-01399-2.
[34] O.N. Senkov, S. Rao, K.J. Chaput, C. Woodward, Compositional effect on microstructure and properties of NbTiZr-based complex concentrated alloys, Acta Mater. 151 (2018) 201–215, https://doi.org/10.1016/j.actamat.2018.03.065.
[35] Y.D. Wu, Y.H. Cai, X.H. Chen, T. Wang, J.J. Si, L. Wang, Y.D. Wang, X.D. Hui, Phase composition and solid solution strengthening effect in TiZrNbMoV high-entropy alloys, Mater. Des. 83 (2015) 651–660, https://doi.org/10.1016/j.matdes.2015.06.072.
[36] G. Chen, H. Yan, Z. Wang, K. Wang, N.I. Yves, Y. Tong, Effects of Mo content on the microstructure and mechanical properties of TiNbZrMox high-entropy alloys, J. Alloys Compd. 930 (2023) 167373, https://doi.org/10.1016/j.jallcom.2022.167373.
[37] L.-Y. Tian, G. Wang, J.S. Harris, D.L. Irving, J. Zhao, L. Vitos, Alloying effect on the elastic properties of refractory high-entropy alloys, Mater. Des. 114 (2017) 243–252, https://doi.org/10.1016/j.matdes.2016.11.079.
[38] H. Zhang, Z. Zhu, H. Huang, T. He, H. Yan, Y. Zhang, Y. Lu, T. Wang, T. Li, Microstructures, mechanical properties, and irradiation tolerance of the Ti–Zr–Nb–V–Mo refractory high-entropy alloys, Intermetallics 157 (2023) 107873, https://doi.org/10.1016/j.intermet.2023.107873.
[39] W. Zhang, P.K. Liaw, Y. Zhang, Science and technology in high-entropy alloys, Sci. China Mater. 61 (2018) 2–22, https://doi.org/10.1007/s40843-017-9195-8.
[40] J. Wang, S. Bai, Y. Tang, S. Li, X. Liu, J. Jia, Y. Ye, L. Zhu, Effect of the valence electron concentration on the yield strength of Ti–Zr–Nb–V high-entropy alloys, J. Alloys Compd. 868 (2021) 159190, https://doi.org/10.1016/j.jallcom.2021.159190.
[41] Z. Fan, H. Wang, Y. Wu, X.J. Liu, Z.P. Lu, Thermoelectric High-Entropy Alloys with Low Lattice Thermal Conductivity, RSC Adv. 6 (2016) 52164–52170, https://doi.org/10.1039/c5ra28088e.
[42] F. Körmann, Y. Ikeda, B. Grabowski, M.H.F. Sluiter, Phonon broadening in high entropy alloys, Npj Comput. Mater. 3 (2017) 36, https://doi.org/10.1038/s41524-017-0037-8.
[43] E.J. Pickering, A.W. Carruthers, P.J. Barron, S.C. Middleburgh, D.E.J. Armstrong, A.S. Gandy, High-entropy alloys for advanced nuclear applications, Entropy 23 (2021) 98, https://doi.org/10.3390/e23010098.
[44] C. Lu, L. Niu, N. Chen, K. Jin, T. Yang, P. Xiu, Y. Zhang, F. Gao, H. Bei, S. Shi, M.-R. He, I.M. Robertson, W.J. Weber, L. Wang, Enhancing radiation tolerance by controlling defect mobility and migration pathways in multicomponent single-phase alloys, Nat. Commun. 7 (2016) 13564, https://doi.org/10.1038/ncomms13564.
[45] F. Granberg, K. Nordlund, M.W. Ullah, K. Jin, C. Lu, H. Bei, L.M. Wang, F. Djurabekova, W.J. Weber, Y. Zhang, Mechanism of radiation damage reduction in equiatomic multicomponent single phase alloys, Phys. Rev. Lett. 116 (2016) 135504, https://doi.org/10.1103/PhysRevLett.116.135504.
[46] P. Bag, Y.-C. Su, Y.-K. Kuo, Y.-C. Lai, S.-K. Wu, Physical properties of face-centered cubic structured high-entropy alloys: effects of NiCo, NiFe, and NiCoFe alloying with Mn, Cr, and Pd, Phys. Rev. Mater. 5 (2021) 085003, https://doi.org/10.1103/PhysRevMaterials.5.085003.
[47] M.-J. Jhong, I.-L. Jen, K.-K. Wang, W.-T. Yen, J.C. Huang, J.S.-C. Jang, K.-C. Hsieh, H.-J. Wu, Nano-structure to Laves phase: reduced thermal conductivity from medium-entropy AlNbV to high-entropy AlNbVCrTi alloys, Materialia 14 (2020) 100889, https://doi.org/10.1016/j.mtla.2020.100889.
[48] H.-P. Chou, Y.-S. Chang, S.-K. Chen, J.-W. Yeh, Microstructure, thermophysical and electrical properties in AlxCoCrFeNi (0≤x≤2) high-entropy alloys, Mater. Sci. Eng. B 163 (2009) 184–189, https://doi.org/10.1016/j.mseb.2009.05.024.
[49] Z. Shen, Y. Su, Z. Liang, X. Long, Review of indentation size effect in crystalline materials: progress, challenges and opportunities, J. Mater. Res. Technol. 31 (2024) 117–132, https://doi.org/10.1016/j.jmrt.2024.06.071.
[50] P. Yvon, F. Carré, Structural materials challenges for advanced reactor systems, J. Nucl. Mater. 385 (2009) 217–222, https://doi.org/10.1016/j.jnucmat.2008.11.026.
[51] K.A. Terrani, S.J. Zinkle, L.L. Snead, Advanced oxidation-resistant iron-based alloys for LWR fuel cladding, J. Nucl. Mater. 448 (2014) 420–435, https://doi.org/10.1016/j.jnucmat.2013.06.041.
[52] A. Vattré, T. Jourdan, H. Ding, M.-C. Marinica, M.J. Demkowicz, Non-random walk diffusion enhances the sink strength of semicoherent interfaces, Nat. Commun. 7 (2016) 10424, https://doi.org/10.1038/ncomms10424.
[53] K.M. Yang, P.Z. Tang, Q. Zhang, H.Y. Ma, E.Q. Liu, M. Li, X. Zhang, J. Li, Y. Liu, T. X. Fan, R. Namakian, Enhanced defect annihilation capability of the graphene/copper interface: an in situ study, Scr. Mater. 203 (2021) 114001, https://doi.org/10.1016/j.scriptamat.2021.114001.
[54] J.L. Du, H.Q. Chen, C. Xu, Y. Fan, Y.H. Qiu, H. Wang, E.G. Fu, Stress of misfit dislocation at Fe/MgO interface drives the annihilation of radiation induced defects, Acta Mater. 210 (2021) 116798, https://doi.org/10.1016/j.actamat.2021.116798.
[55] X.-J. Hua, P. Hu, H.-R. Xing, J.-Y. Han, S.-W. Ge, S.-L. Li, C.-J. He, K.-S. Wang, C.-J. Cui, Development and property tuning of refractory high-entropy alloys: a review, Acta Metall. Sin. (Engl. Lett.) 35 (2022) 1231–1265, https://doi.org/10.1007/s40195-022-01382-x.
[56] C. Lee, F. Maresca, R. Feng, Y. Chou, T. Ungar, M. Widom, K. An, J.D. Poplawsky, Y.-C. Chou, P.K. Liaw, W.A. Curtin, Strength can be controlled by edge dislocations in refractory high-entropy alloys, Nat. Commun. 12 (2021) 5474, https://doi.org/10.1038/s41467-021-25807-w.